Abo-Hamad, A., M. Phadatare, and J. Örtegren. 2026. Urea-Assisted Porosification of Silicon Microparticles. In *Silicon for the chemical and solar industry XVIII,* edited by M. Tangstad, H. Rong, A. Valderhaug, B. Andresen, H. Dalaker, and I. G. Page. Kristiansand, Norway, September 7–10, 2026. https://doi.org/10.55669/oa900816

Urea-Assisted Porosification of Silicon Microparticles

Ali Abo-Hamad[1], Manisha Phadatare[1], and Jonas Örtegren[1]
[1]Department of Engineering, Mathematics and Science Education (IMD), Mid Sweden University, Sundsvall, SE-851 70, Sweden, jonas.ortegren@miun.se

Keywords: Porous silicon, Urea etching, Mesoporosity, Surface chemistry

Abstract – Fluorine-free routes for producing porous silicon are attractive for safer and more scalable silicon processing. In this work, urea-assisted thermochemical porosification of polycrystalline silicon microparticles was investigated at 400 °C, with emphasis on urea loading and the thermal sequence leading to pore formation. Silicon microparticles were blended with urea at urea-to-silicon (Urea:Si) mass ratios of 0.5:1, 1:1, 2:1, and 4:1, followed by a staged thermal protocol involving urea melting at 135 °C and subsequent treatment at 400 °C. Urea loading was evaluated using nitrogen sorption, BJH pore-size analysis, SEM, and EDS. The 2:1 Urea:Si blend produced a sharp increase in porosity, reaching a BET surface area of 25.7 $m^2 g^{-1}$ and a pore volume of 0.039 $cm^3 g^{-1}$, while further increasing the ratio to 4:1 gave only minor additional improvement. The 2:1 blend was selected and further examined using mercury porosimetry and TG/DSC. TG/DSC showed that pristine silicon remains mass-stable, whereas the Urea:Si mixture undergoes substantial mass loss during the 135 °C hold and displays lower-temperature DSC events than pure urea. These results suggest coupled gas-solid surface modification and stress-assisted pore formation during heating to 400 °C.

1. INTRODUCTION

Porous silicon has evolved into a versatile silicon-based platform because its high internal surface area, tuneable pore architecture, versatile surface chemistry, photonic response, and structural void space can be tailored for different functions. These characteristics enable refractive-index and photoluminescence-based transduction in optical biosensing (Moretta et al., 2021), improved stability and functionality in polymer-modified porous silicon sensors (Nocerino et al., 2024), enhanced biomolecule loading and sensitivity in point-of-care, wearable, and implantable biosensors (Sánchez-Salcedo et al., 2025), and support drug delivery, tissue engineering, and implant-related applications in biomedical systems (Kang et al., 2025) In energy-related applications, the combination of accessible active sites, short diffusion distances, and internal void space is advantageous for electrocatalysis and supercapacitors (M. Wang et al., 2025), while in Li-ion batteries porous silicon architectures can partially accommodate silicon volume expansion and improve electrochemical accessibility compared with bulk silicon (Cheng et al., 2023). More broadly, porous silicon is regarded as a structure-sensitive material platform whose performance depends on coupled control of pore geometry, crystallinity, connectivity, and surface termination (Y. Wang & Wang, 2026).

Despite this broad potential, the preparation of porous silicon remains strongly linked to wet-chemical dissolution routes that can complicate scalability, safety, and feedstock flexibility. Electrochemical anodization is still regarded as a cornerstone method because it enables precise control over pore morphology through current density, electrolyte composition, and etching time; however, it commonly relies on hydrofluoric acid (HF)-based electrolytes and is

most naturally suited to wafer-based processing (Y. Wang & Wang, 2026). Similarly, many biosensing-oriented porous silicon structures are fabricated by electrochemical etching in HF-based media, where pore size and film thickness must be optimized for analyte infiltration and sensor performance (Sánchez-Salcedo et al., 2025). In biomedical porous silicon fabrication, electrochemical etching also remains the dominant route, with HF-based electrolytes used to dissolve silicon into hexafluorosilicate species and generate the porous matrix (Kang et al., 2025). Although such methods are highly effective, the need for hazardous fluorine-containing chemistry, wafer-based configurations, and careful post-processing creates limitations for large-scale or powder-compatible production. In energy-storage applications, additional challenges arise because many porous silicon routes involve high temperatures, expensive precursors, complex procedures, or hazardous chemicals, which can limit practical scalability (Abo-Hamad et al., 2026). Recent reviews also note that porous silicon obtained through electrochemical corrosion or high-temperature processing can show complex, difficult-to-control pore structures, affecting surface utilization and mass transport (M. Wang et al., 2025). These limitations motivate the development of fluorine-free, powder-compatible, and thermochemically tuneable routes that can generate accessible porosity while preserving the crystalline silicon framework and enabling controllable surface modification. Such powder-compatible approaches may also offer advantages for future integration with existing silicon powder-processing workflows, although their practical scalability depends on heat and mass transfer, reagent utilization, energy demand, and process configuration.

Urea offers an attractive chemical entry point into fluorine-free silicon porosification because it is inexpensive, widely available, and thermally active over a temperature range compatible with low-temperature silicon processing. Its decomposition, however, is not a single-step release of gaseous products. Urea first melts near 133 °C and then undergoes a temperature-dependent sequence of evaporation, decomposition, condensation, and secondary reactions. The primary thermolysis pathway is commonly described as:

$$(H_2N)_2CO \rightarrow NH_3 + HNCO \quad (1)$$

followed by hydrolysis of isocyanic acid:

$$HNCO + H_2O \rightarrow NH_3 + CO_2 \quad (2)$$

and by secondary reactions that generate condensed intermediates such as biuret and cyanuric acid:

$$(H_2N)_2CO + HNCO \rightarrow (H_2NCO)_2NH \quad (3)$$

$$(H_2NCO)_2NH + HNCO \rightarrow CYA + NH_3 \quad (4)$$

$$3HNCO \rightarrow CYA \quad (5)$$

where CYA denotes cyanuric acid. Further reactions can form ammelide and ammeline through NH_3-containing pathways, indicating that urea decomposition generates not only volatile species but also transient condensed phases (Zhu et al., 2021).

The temperature dependence of these reactions is central to the present process. Thermogravimetric and mass-spectrometric studies have shown that below 160 °C, urea decomposition is limited and the dominant process is slow evaporation of molten urea, whereas between 180 and 200 °C biuret formation becomes significant. Above 200 °C, urea and biuret decompose more rapidly, while cyanuric-acid-type residues become increasingly important and later decompose at higher temperature, particularly above approximately 330 °C (Zhu et al., 2021). Schaber and co-workers (Schaber et al., 2004) further showed that urea pyrolysis in an open vessel proceeds through competing temperature-dependent pathways, with HNCO reacting with intact urea to form biuret, followed by formation of cyanuric acid, ammelide, and ammeline; Tischer and co-workers (Tischer et al., 2019) later emphasized the role of equilibrium processes and explained the liquefaction and re-solidification of biuret in the 193-230 °C range through eutectic behavior with urea. These studies imply that, during urea-assisted silicon treatment, the active chemical environment is likely produced

progressively through melting, redistribution, gas evolution, and transient solid or viscous intermediate formation rather than by a single decomposition event at the final treatment temperature.

The relevance of urea-derived species to silicon porosification is supported by the broader chemistry of silicon in ammonia-containing environments. Ammonium hydroxide-based etchants have long been used in silicon micromachining, where $NH_4OH–H_2O$ solutions can anisotropically etch monocrystalline silicon while showing high selectivity toward SiO_2, Si_3N_4, and highly boron-doped silicon (Schnakenberg et al., 1990). Selective etching of silicon in aqueous ammonia has also been demonstrated under electrochemical bias, where the formation of passivating oxide films and the relative behavior of n- and p-type regions depend sensitively on the applied potential (Chen et al., 1995). In NH_3 solution, Si(111) etching has been monitored through hydrogen evolution, indicating that alkaline silicon dissolution is coupled to surface oxidation/reduction processes, represented in that study in simplified form by:

$$Si + 4H_2O \rightarrow Si^{4+} + 4OH^- + 2H_2 \quad (6)$$

with dissolved oxygen found to alter both surface morphology and etching rate. High dissolved oxygen concentrations produced etch pits, whereas oxygen removal led to flatter hydrogen-terminated Si(111) surfaces; the etching rate decreased from 25 ± 1 to 19 ± 1 nm min^{-1} in the presence of dissolved oxygen (Fukidome & Matsumura, 2000). Ammonia–peroxide mixtures used in Radio Corporation of America (RCA) cleaning further illustrate the coupled nature of oxidation and dissolution: silicon can be oxidized to a thin chemical oxide while ammonia participates in oxide redissolution, and deviations in oxidant concentration can produce localized alkaline etching and roughening (Knotter et al., 2000; Lee & Raghavan, 1999). At the molecular scale, reactions between SiO_2 and NH_3 have also been reported to form $SiO_2–NH_3$ complexes and $H_2NSiOOH$-type species, suggesting that ammonia can interact not only with elemental silicon but also with oxidized silicon surfaces (Zhou & Chen, 2001).

These observations are particularly relevant because urea decomposition can supply NH_3 and HNCO locally within a silicon powder bed, while oxygen and residual moisture can simultaneously influence surface oxidation, oxide dissolution, and nitrogen incorporation. In this context, urea is not simply a gas precursor; it is a thermally evolving chemical medium that can wet silicon particles, generate volatile species, form condensed intermediates, and create localized pressure or stress as those intermediates expand, crystallize, or decompose. This combination provides a plausible basis for a dual porosification pathway in which chemical surface modification and mechanically assisted disruption occur together (Abo-Hamad et al., 2026). Such a view is consistent with the known behavior of urea-derived phases and with ammonia-based silicon surface chemistry, although the actual chemistry within the powder bed is likely more complex and may also involve local variations in oxygen partial pressure and moisture content, HNCO adsorption, oxide transformation, and transient Si–O–N-type surface environments. These possibilities are regarded here as potential secondary pathways rather than experimentally established reactions. It remains important to resolve how these processes unfold under the specific staged heating program used for silicon microparticle treatment.

In our previous work (Abo-Hamad et al., 2025), we introduced urea-assisted thermochemical treatment as a fluorine-free route for producing porous silicon microparticles from metallurgical-grade polycrystalline silicon. That study evaluated temperature and container environment and showed that urea treatment transformed dense pristine silicon microparticles with a Brunauer-Emmett-Teller (BET) surface area of 2.3 $m^2 g^{-1}$ into porous silicon with surface areas as high as 26.7 $m^2 g^{-1}$. Under atmospheric conditions, the most

pronounced porosity was obtained at 400 °C, where the surface area reached 25.7 $m^2\ g^{-1}$ and the pore volume reached 0.039 $cm^3\ g^{-1}$, with an etching yield of 17.5%, an average etching rate of 14.6 mg h^{-1}, and a pore formation efficiency of about 43%. In contrast, treatments at 600 and 800 °C produced porosity close to that of pristine silicon, which was attributed to rapid and intense urea decomposition that limited sustained gas-solid interaction. That study also showed that urea treatment produced temperature- and environment-dependent oxidation and nitrogen incorporation, with Si–N, NH_2/NH_3^+, and NO_x-type species detected under selected conditions. More detailed surface-sensitive characterization combining X-ray photoelectron spectroscopy (XPS) with complementary techniques such as Fourier-transform infrared spectroscopy (FTIR), Raman spectroscopy, and time-of-flight secondary ion mass spectrometry (ToF-SIMS) could further resolve Si–O, Si–N, Si–O–N, and NH_x-type surface environments in future studies.

A subsequent study extended this strategy to porous silicon microparticles for Li-ion battery anodes and provided more direct support for a coupled porosification mechanism (Abo-Hamad et al., 2026). Therein, urea-assisted treatment produced particles with open pores and cavities, increased oxygen content, nitrogen-containing surface functionalities, and a substantial increase in BET surface area from 2.3 to 26.7 $m^2\ g^{-1}$. The observed morphology was interpreted as arising from both mechanical effects, associated with gas evolution and transient urea-derived phases, and chemical effects, associated with NH_3/HNCO-mediated surface modification, oxidation, and possible oxide transformation. Control experiments further showed that thermal exposure alone did not reproduce the porosity, while chemically minimized and mechanically minimized conditions generated only partial features; the full urea-assisted treatment produced the strongest mesoporosity, supporting a dual-effect mechanism in which chemically driven surface modification and stress-assisted structural disruption act together.

Despite these advantages, two mechanistic questions remain open for the 400 °C condition. First, the influence of urea loading has not been isolated at this selected temperature, even though the amount of urea should govern the balance between molten-phase redistribution, gas generation, intermediate formation, and silicon surface accessibility. Too little urea may provide insufficient chemical and mechanical driving force, whereas excessive urea may promote rapid mass loss, shielding, agglomeration, or inefficient gas-solid contact. Second, the thermal pathway of urea in direct contact with pristine silicon under the exact staged heating protocol remains unresolved. This distinction is important because urea alone is known to decompose through multistep pathways, but the silicon powder bed may modify the apparent onset, extent, and stability of urea-derived events by dispersing molten urea over particle surfaces and confining intermediate phases within interparticle voids.

In this work, we address these questions by fixing the treatment temperature at 400 °C and varying the Urea:Si mass ratio from 0.5:1 to 4:1. The effect of urea loading is evaluated using nitrogen sorption, Barrett-Joyner-Halenda (BJH) pore-size analysis, scanning electron microscopy (SEM), and energy-dispersive X-ray spectroscopy (EDS) to determine how urea amount controls porosity development and surface composition. The Urea:Si (2:1 mass ratio) blend is then selected for further analysis using mercury porosimetry and thermogravimetry/differential scanning calorimetry (TG/DSC) to connect pore-network accessibility with the staged thermal evolution of urea in contact with silicon. By comparing pristine silicon, pure urea, and the Urea:Si mixture under the same heating protocol, this work aims to identify when the active chemical and mechanical events occur and how they relate to pore formation. The purpose is therefore not to re-establish the general feasibility of urea-

assisted silicon etching, but to clarify how urea loading and staged thermal decomposition govern fluorine-free porosification at 400 °C.

2. Materials and Methods

2.1 Materials

Metallurgical-grade polycrystalline silicon microparticles were used as the silicon feedstock. The powder was commercially supplied as SicoMill Grade 2E by Vesta Si Sweden AB (SKF Group Company, Sweden), batch drum no. 35512, with a reported purity of 98 to 99% and an average particle size of approximately 4.6 to 5 µm. The silicon powder was used as received without further purification or pretreatment. Urea (ACS reagent grade, ≥99.5%) was purchased from Sigma-Aldrich and used as the thermochemical porosification agent. Deionized water and ethanol were used for cleaning and post-treatment washing.

2.2 Synthesis of porous silicon

Silicon microparticles were blended with urea at Urea:Si mass ratios of 0.5:1, 1:1, 2:1, and 4:1. The powders were mixed manually using an agate mortar and pestle for 10 min to promote homogeneous distribution of urea throughout the silicon powder bed. Before use, all tools and containers were rinsed with deionized water and ethanol and dried. The untreated pristine silicon powder is denoted as PrSi, while the porous silicon obtained from the selected Urea:Si (2:1 mass ratio) mixture is denoted as PoSi.

The blended powders were thermally treated under ambient laboratory air at atmospheric pressure in ceramic crucibles using a programmable Nabertherm furnace. The heating program consisted of two stages. First, the mixture was heated to 135 °C at 5 °C min^{-1} and held for 1 h to melt urea and promote redistribution within the silicon powder bed. Second, the temperature was increased to 400 °C at 10 °C min^{-1} and maintained for 12 h. This temperature was selected based on previous optimization of urea-assisted silicon porosification, where 400 °C under atmospheric conditions produced the most pronounced mesoporosity (Abo-Hamad et al., 2025).

After thermal treatment, the powders were allowed to cool to room temperature and were washed repeatedly with boiling deionized water to remove residual urea and soluble urea-derived by-products. The powders were then filtered and dried prior to characterization.

2.3 Characterization

Nitrogen adsorption-desorption measurements were performed using a TriStar II Plus analyzer (Micromeritics) to determine the textural properties of PrSi and the treated samples. Before analysis, the powders were degassed under nitrogen flow at 300 °C for 1 h. The specific surface area was calculated using the Brunauer-Emmett-Teller (BET) method, and the pore-size distribution was estimated using the Barrett-Joyner-Halenda (BJH) model. Measurements were performed in triplicate, and the reported BET surface area and pore volume values represent the mean of three measurements, with error bars indicating the standard deviation.

Surface morphology and elemental composition were analyzed by scanning electron microscopy (SEM) and energy-dispersive X-ray spectroscopy (EDS) using a TESCAN MAIA3 Triglav™ SEM equipped with EDS. SEM was used to examine changes in particle morphology, surface roughness, and pore formation as a function of urea loading, while EDS was used to evaluate changes in elemental composition after treatment.

Thermogravimetric and differential scanning calorimetry analysis was performed using a NETZSCH STA 449 F1 instrument in simultaneous TG/DSC mode. Measurements were

carried out for PrSi, pure urea, and the selected Urea:Si (2:1 mass ratio) mixture using alumina crucibles. The applied program followed the synthesis sequence: heating from room temperature to 135 °C at 5 °C min^{-1}, holding at 135 °C for 1 h, heating to 400 °C at 10 °C min^{-1}, and holding at 400 °C for 2 h for analytical tracking of the main thermal events. The measurements were conducted under an N_2/O_2 flow of 50 mL min^{-1}, together with N_2 protective gas at 20 mL min^{-1}, to mimic the oxidizing air-containing environment used during the atmospheric thermal treatment. The TG signal was used to follow mass changes, while the DSC signal was used to identify thermal events associated with urea melting, decomposition, and removal of urea-derived intermediates.

Mercury intrusion porosimetry was performed using a Micromeritics AutoPore IV 9500 instrument to assess pore-network accessibility in PrSi and PoSi. Measurements were carried out using a powder penetrometer with a 3 mL cup volume and 0.412 mL stem/internal volume, and the intrusion data were used to compare accessible pore volume and pore-size distribution beyond the mesopore range probed by nitrogen sorption.

2.4 Data analysis

The influence of urea loading was evaluated by comparing BET surface area, BJH pore-size distribution, SEM morphology, and EDS elemental composition across the Urea:Si series. The 2:1 Urea:Si sample was selected for additional mechanistic analysis because it produced nearly the full porosity enhancement observed at higher urea loading while avoiding excess reagent. TG/DSC data were used to compare the thermal behavior of PrSi, pure urea, and the Urea:Si mixture under the same staged heating program, while mercury intrusion porosimetry was used to complement nitrogen sorption by probing larger-scale accessible pore features.

3. Results and Discussion

Our previous work (Abo-Hamad et al., 2025) established urea-assisted thermochemical treatment as a fluorine-free route for porosifying polycrystalline silicon microparticles and identified two particularly informative processing conditions: confined treatment at 220 °C and atmospheric treatment at 400 °C. The confined 220 °C route was later examined through control experiments, supporting a dual-effect mechanism involving chemical surface modification and stress-assisted structural disruption (Abo-Hamad et al., 2026). The present work focuses on the other key condition, namely the 400 °C atmospheric treatment, and examines how urea content controls pore development. Urea:Si mass ratios of 0.5:1, 1:1, 2:1, and 4:1 were compared by nitrogen sorption, BJH analysis, SEM, and EDS, while the selected 2:1 composition was further studied by mercury intrusion porosimetry and TG/DSC.

3.1 Urea-content dependence of mesopore development at 400 °C

Nitrogen sorption was first used to evaluate how the initial urea content influences pore formation during atmospheric treatment at 400 °C. PrSi microparticles showed only limited nitrogen uptake across the full relative-pressure range, consistent with the dense and weakly porous nature of the starting material (Figure 1a). The BJH pore-size distribution of PrSi was also weak and poorly defined, confirming that the untreated powder does not contain a developed mesopore network in the range probed by nitrogen sorption (Figure 1b). Consistently, PrSi exhibited a low BET surface area of 2.4 m^2 g^{-1} and a total pore volume of only 0.0031 cm^3 g^{-1} (Figure 1c).

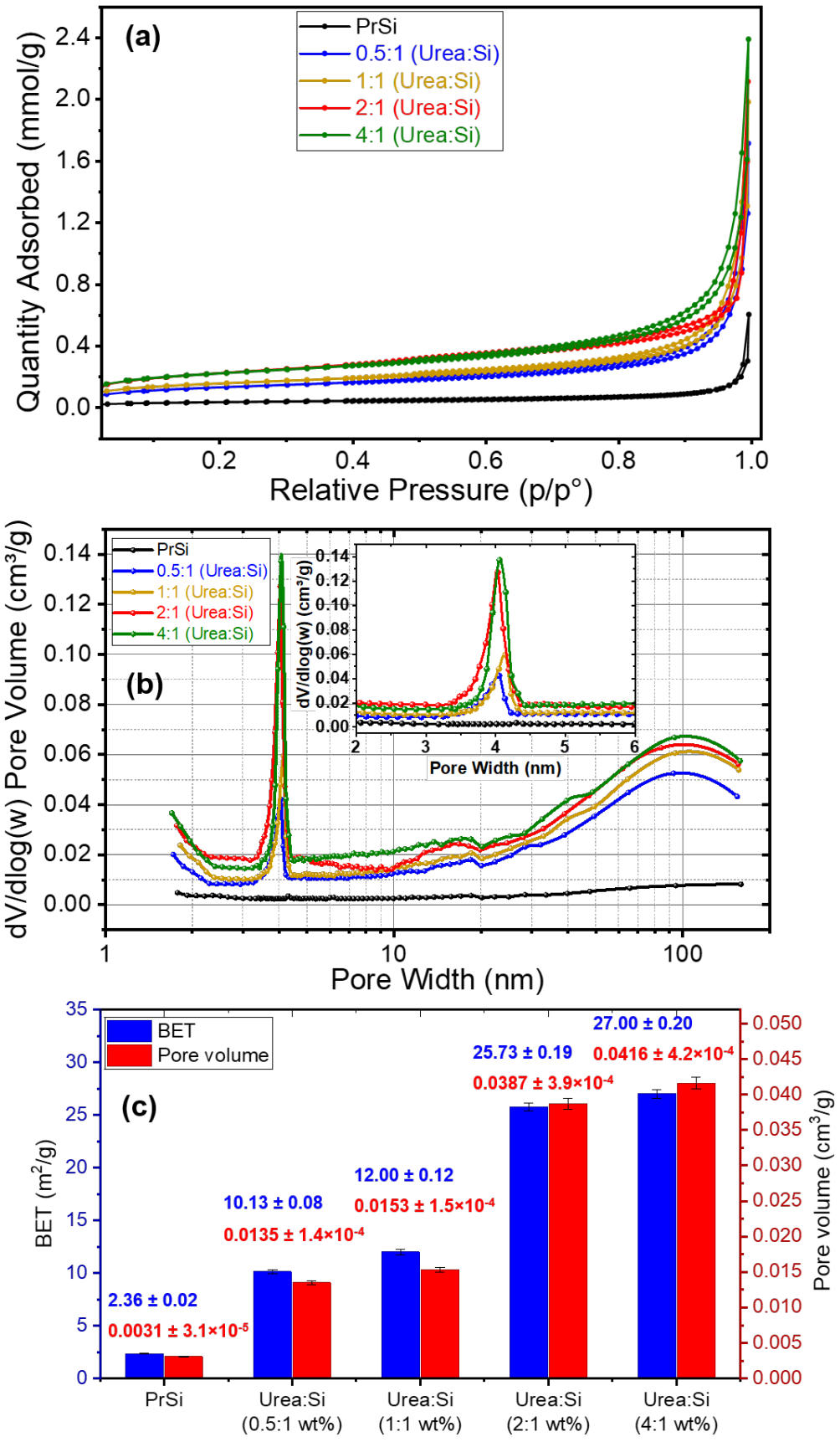

Figure 1. Effect of urea content on pore development in silicon microparticles treated at 400 °C. (a) Nitrogen adsorption-desorption isotherms, (b) BJH pore-size distributions, with inset highlighting the dominant ~4 nm mesopore population, and (c) BET surface area and pore volume of PrSi and Urea:Si-treated samples. Values in (c) are presented as mean ± standard deviation (n = 3).

After urea-assisted treatment, the adsorption capacity increased for all Urea:Si ratios, demonstrating that the 400 °C treatment generates additional accessible porosity. Even the lowest urea loading, 0.5:1 Urea:Si, increased the BET surface area to 10.1 $m^2 g^{-1}$ and the pore volume to 0.014 $cm^3 g^{-1}$, corresponding to roughly a fourfold increase relative to PrSi. Increasing the urea content to 1:1 produced a further but moderate increase, with a BET surface area of 12.0 $m^2 g^{-1}$ and pore volume of 0.015 $cm^3 g^{-1}$. This indicates that low urea loadings are sufficient to initiate porosity formation, but not enough to fully develop the accessible pore network.

A more pronounced transition occurred when the Urea:Si ratio was increased to 2:1. At this composition, the BET surface area rose sharply to 25.7 $m^2 g^{-1}$, while the pore volume increased to 0.039 $cm^3 g^{-1}$. Compared with PrSi, this corresponds to an approximately 11-fold increase in surface area and a 12.5-fold increase in pore volume. The adsorption isotherm also showed substantially higher nitrogen uptake, particularly at elevated relative pressures, indicating a much larger accessible void volume after treatment. This sharp increase suggests that a critical urea content is required to generate sufficient volatile and transient urea-derived species for effective pore development.

Further increasing the urea loading to 4:1 gave the highest numerical BET surface area and pore volume, 27.0 $m^2 g^{-1}$ and 0.042 $cm^3 g^{-1}$, respectively. However, the gain relative to the 2:1 sample was small, only about 5% in surface area and 8% in pore volume. Thus, the porosity development does not scale linearly with urea content. Instead, the sorption data indicate that the system approaches a near-saturation regime after the 2:1 ratio, where additional urea provides only a limited improvement in accessible porosity. This plateau may indicate that, beyond the 2:1 ratio, additional urea provides little further benefit because gas transport becomes more restricted and urea-derived intermediates may accumulate, reducing access to fresh Si surface.

The BJH pore-size distributions provide further insight into this behavior (Figure 1b). All urea-treated samples show a distinct mesopore population centered at approximately 4.0-4.1 nm, whereas PrSi exhibits only a weak background response. This dominant feature is highlighted in the inset of Figure 1b. Increasing the urea content does not substantially shift the position of this main peak; instead, its intensity increases strongly from 0.5:1 to 2:1 and then changes only modestly at 4:1. This indicates that urea loading primarily controls the extent and accessibility of this dominant mesopore population, rather than changing its characteristic pore width. In addition, the distributions show a broader, less-defined contribution at larger pore widths, extending toward ~100 nm, particularly for the urea-treated samples. This feature should be interpreted cautiously because BJH analysis above the mesopore range is sensitive to near-saturation adsorption and may include interparticle or packing-related contributions. Nevertheless, it agrees with previous control experiments showing that full urea-assisted treatment can combine a dominant ~4 nm mesopore population with secondary larger pore/void features, whereas crack- and void-dominated conditions give stronger large-pore responses (Abo-Hamad et al., 2026).

Taken together, the nitrogen sorption results show that urea content is a decisive parameter in the atmospheric 400 °C porosification route. Low urea loadings initiate surface and pore development, while the transition from 1:1 to 2:1 marks the major increase in accessible mesoporosity. The small additional gain at 4:1 indicates that excessive urea is not proportionally beneficial, likely because pore formation becomes limited by silicon surface accessibility, gas-solid contact, or the removal of urea-derived intermediates rather than by urea availability alone. Therefore, the 2:1 Urea:Si composition represents a practical high-

porosity condition, providing nearly the full porosity enhancement observed at higher urea loading while avoiding unnecessary excess reagent.

3.2 Morphological and compositional evolution with urea content

SEM and EDS analyses were used to examine whether the textural changes identified by nitrogen sorption are reflected in the particle morphology and surface composition. PrSi consists of angular microparticles with compact, faceted surfaces and no clear open-pore network at the SEM scale (Figure 2). The higher-magnification images show mostly smooth surface regions with only minor surface debris or native roughness, consistent with the low nitrogen uptake, weak BJH response, and low BET surface area discussed above.

After urea-assisted treatment at 400 °C, all Urea:Si compositions exhibit pronounced morphological modification relative to PrSi. At the lowest urea content, 0.5:1 Urea:Si, the particles already show a roughened and granular surface, together with visible cracks and local voids. Increasing the ratio to 1:1 and 2:1 produces more extensive surface disruption, with roughened domains, open cavities, and pore-like features distributed across the particle surfaces. At 4:1, the surface remains highly roughened and porous-looking, although the morphology does not show a simple linear increase in pore development compared with the 2:1 sample. This agrees with the nitrogen sorption data, where increasing the urea loading from 2:1 to 4:1 resulted only in a modest additional increase in BET surface area and pore volume.

The treated morphologies are consistent with the dual chemical-mechanical mechanism proposed in our earlier work (Abo-Hamad et al., 2025), where urea-derived species contribute to chemical surface modification while gas evolution and transient condensed phases may generate local stresses within defects, interparticle spaces, or pre-existing voids. Control experiments previously showed that thermal treatment alone retained a dense PrSi-like morphology, whereas the full urea-assisted process produced the strongest surface disruption and nanoscale void formation (Abo-Hamad et al., 2026). The present SEM images therefore support the same picture for the 400 °C atmospheric route, showing surface roughening, cracking, and pore opening across all urea-containing samples.

Because SEM probes only selected local regions, it should be used qualitatively rather than as a direct ranking of porosity among the treated samples. Individual particles can differ in crystal facets, defect density, local urea contact, and gas-escape pathways. Thus, SEM confirms the morphological transformation from compact PrSi to roughened, cracked, and void-containing particles, while the quantitative urea-content trend is more reliably determined from nitrogen sorption.

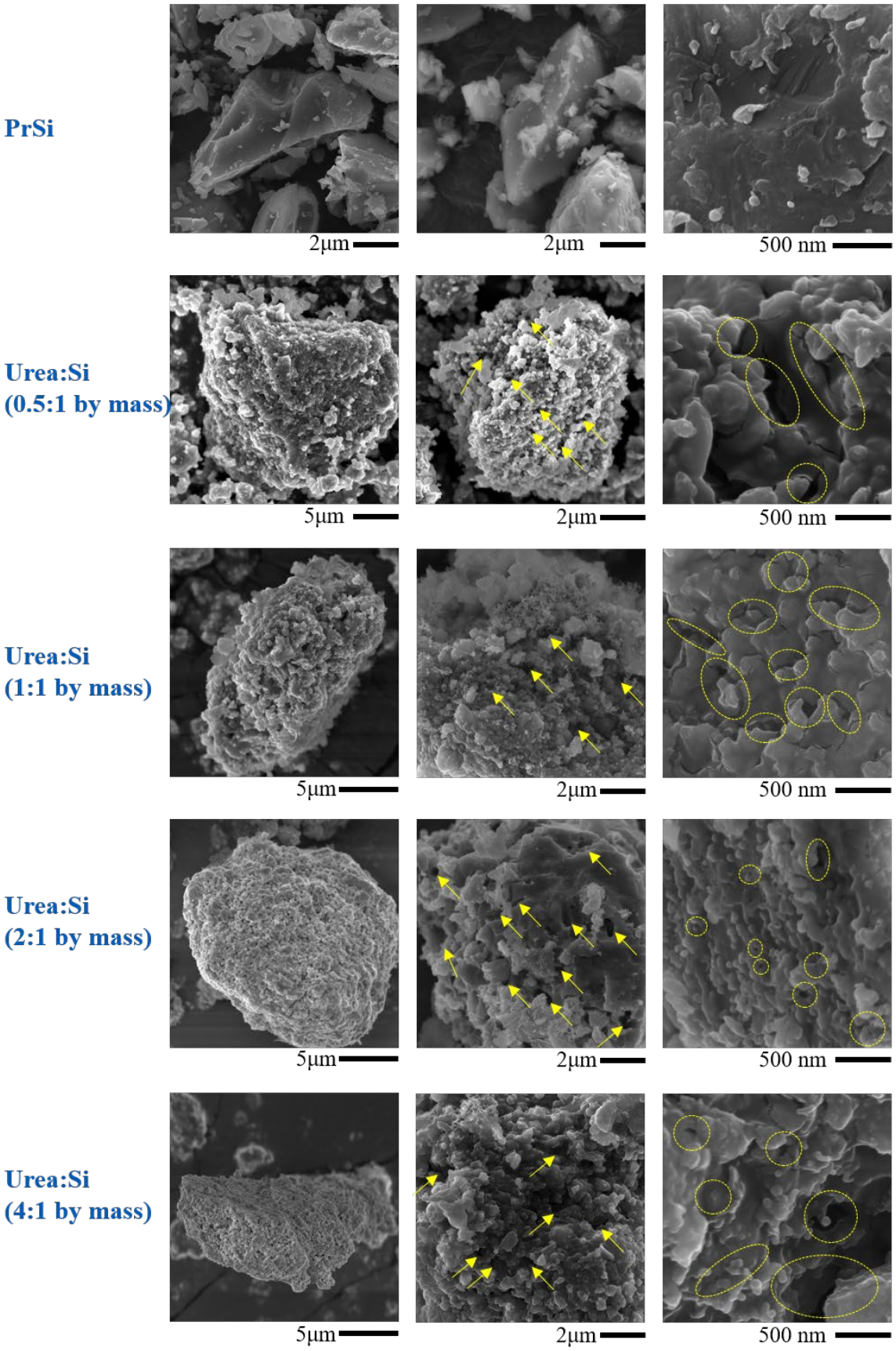

Figure 2. SEM morphology of PrSi and Urea:Si-treated samples. Arrows and dashed outlines highlight representative cavity- and pore-like features visible at higher magnification.

EDS mapping further confirms that the urea treatment modifies the surface composition (Figure 3). In PrSi, the EDS scan shows a dominant Si signal with only 2.5 wt% O, consistent with a native oxide layer on the untreated silicon surface. After treatment, the oxygen signal increases systematically with urea content: 5.5 wt% for 0.5:1, 8.2 wt% for 1:1, 11.4 wt% for 2:1, and 11.8 wt% for 4:1 Urea:Si. The corresponding Si signal decreases from 97.5 wt% in PrSi to 94.5, 91.8, 88.6, and 88.2 wt%, respectively. This progressive increase in oxygen is consistent with greater oxygen-containing surface modification during the 400 °C treatment; however, EDS does not provide chemical-state information and therefore cannot distinguish specific Si–O or related bonding environments.

The oxygen maps show that O is not distributed as a uniform bulk component but is more visible at particle edges, roughened surfaces, cracks, and boundary regions. Such spatial localization is consistent with preferential oxygen enrichment at more exposed and structurally disrupted regions, where edges and pore walls provide greater accessible surface area than smooth facets. The increase in oxygen content therefore likely reflects both chemical modification and the increased surface area generated during porosification. This interpretation is consistent with our previous temperature-screening study, where the 400 °C atmospheric sample showed both high porosity and strong oxygen incorporation; the increased oxygen content was attributed to enhanced surface exposure together with sufficient residence of urea-derived reactive species to interact with the silicon surface (Abo-Hamad et al., 2025).

Importantly, the oxygen increase follows the same general trend as the nitrogen sorption data. The largest compositional shift occurs as the urea content is increased toward the 2:1 ratio, whereas the difference between 2:1 and 4:1 is small. This plateau-like behavior suggests that beyond a certain urea loading, the accessible silicon surface and the efficiency of gas-solid interaction become limiting factors. Additional urea may generate more volatile products, but it does not proportionally increase the accessible oxidized or porous surface. Thus, the SEM/EDS results support the conclusion from nitrogen sorption: the 2:1 Urea:Si composition provides a high degree of surface modification and pore development, while further increasing urea content gives only limited additional benefit.

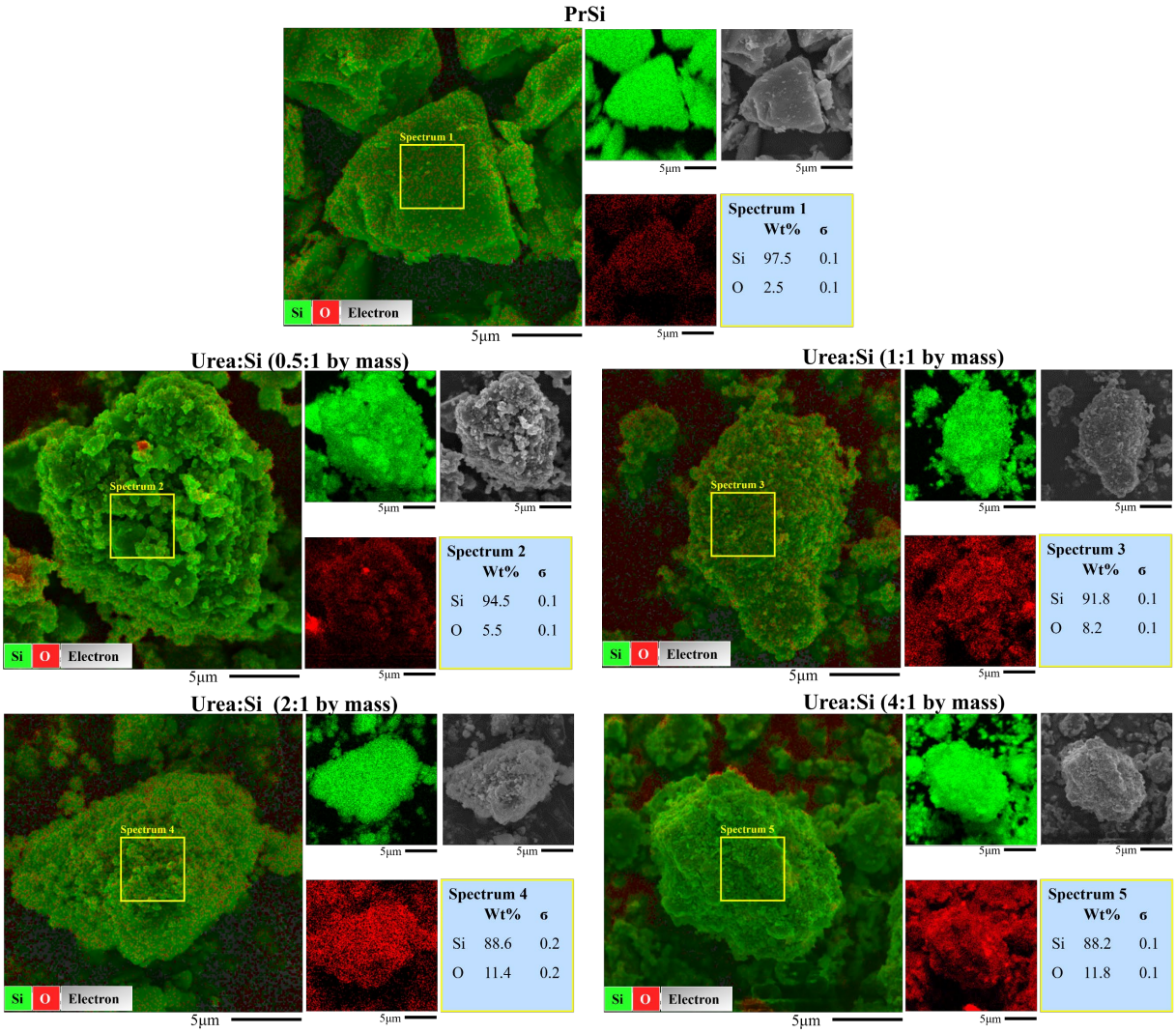

Figure 3. EDS elemental mapping of PrSi and Urea:Si-treated samples. For each sample, the merged Si/O map is shown on the left, with Si in green and O in red. The right-side panels show the separated Si signal and SEM image above, and the separated O signal with local Si/O quantification below. Boxed regions indicate the areas used for EDS quantification.

3.3 Pore-network accessibility of the selected 2:1 Urea:Si-derived PoSi

Mercury intrusion porosimetry was used to complement nitrogen sorption by probing larger accessible pore-throat features in PrSi and the PoSi obtained from the 2:1 Urea:Si treatment. While nitrogen sorption is most sensitive to the mesopore range, mercury intrusion provides information on larger accessible voids, cracks, cavities, and pore throats. For powder samples, the response may also include interparticle voids associated with particle packing; therefore, the data are interpreted here as a comparison of larger-scale pore-network accessibility rather than solely as internal particle porosity. Accordingly, the absolute intrusion volumes and larger pore-size features should not be interpreted exclusively as intraparticle porosity.

PrSi shows a limited intrusion response, with a cumulative intrusion of approximately 0.32 mL g^{-1} and a main differential feature centered near 1 µm (Figure 4). Since PrSi appears compact and non-porous in SEM and exhibits only weak nitrogen uptake, this micron-scale intrusion is most likely dominated by packing-related voids between irregularly shaped silicon particles rather than by a developed internal pore network.

PoSi, however, exhibits a substantially stronger intrusion response. The cumulative intrusion increases to approximately 0.84 mL g^{-1}, corresponding to about 2.6 times the value measured for PrSi (Figure 4). The differential intrusion curve shows a dominant feature near 0.84 µm, together with an additional contribution extending roughly from 150 to 600 nm, which is largely absent in PrSi. This indicates that the 2:1 Urea:Si treatment introduces new accessible pore/void features at submicron length scales, in addition to the larger interparticle void contribution common to powders.

Together with the nitrogen sorption data, the mercury intrusion results suggest that PoSi develops a hierarchical pore structure. Nitrogen sorption resolves a dominant mesopore population near 4 nm, and a broader, less-defined contribution in the ~80-100 nm range, while mercury intrusion reveals larger accessible features from roughly 0.15 to 1 µm. This multiscale pore response is consistent with the SEM observations of roughened surfaces, cracks, and open voids, and is also consistent with previous control experiments suggesting that urea-derived chemical surface modification and gas/intermediate-driven structural disruption may act together during porosification (Abo-Hamad et al., 2026).

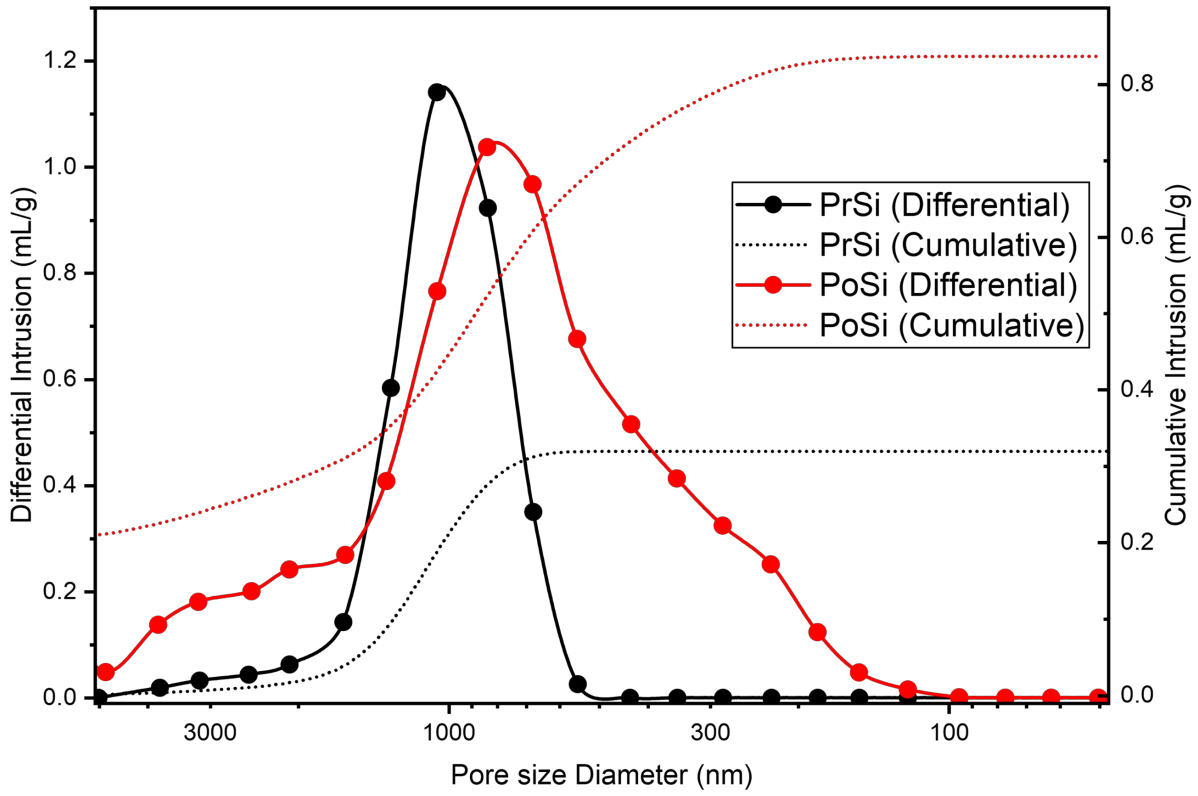

Figure 4. Differential and cumulative mercury intrusion curves comparing PrSi and PoSi obtained from the 2:1 Urea:Si treatment.

3.4 Thermal sequence of urea transformation in contact with silicon

TG/DSC analysis was used to resolve how urea evolves during the staged thermal treatment and how this behavior changes when urea is mixed with PrSi. The full TG response and temperature profile are shown in Figure 5a, the corresponding DSC traces as a function of time are shown in Figure 5b, and the dynamic region between 135 and 400 °C, where the main decomposition events occur, is enlarged in Figure 5c. The main mass changes and DSC features are summarized in Table I.

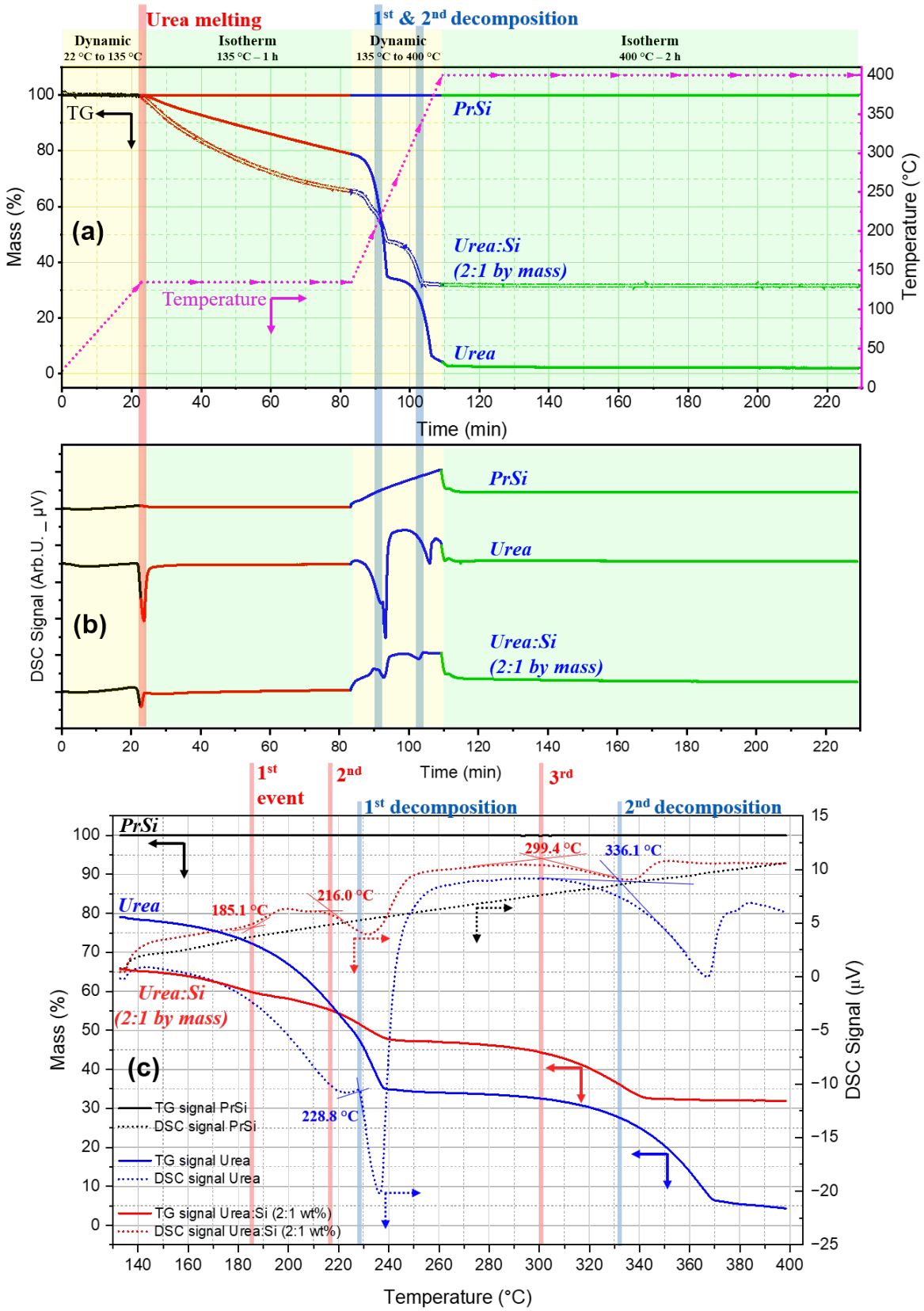

Figure 5. TG/DSC response of PrSi, urea, and Urea:Si (2:1 mass ratio). (a) TG curves and temperature profile during the full staged thermal program, (b) DSC traces versus time, and (c) enlarged TG/DSC comparison during the dynamic 135-400 °C region, showing shifted urea-derived thermal events in the Urea:Si mixture.

Table I: Summary of TG mass changes and DSC features during the staged thermal program

Sample	Thermal segment	Mass change (%)	Residual mass (%)	Main DSC feature
PrSi	1, Dynamic, 22 to 135 °C at 5 °C/min	-0.03	99.97	-
	2, Isothermal, 135 °C for 1 h	-0.01	99.96	-
	3, Dynamic, 135 to 400 °C at 10 °C/min	-0.02	99.94	-
	4, Isothermal, 400 °C for 2 h	+0.07	100.01	-
Urea	1, Dynamic, 22 to 135 °C at 5 °C/min	-0.09	99.91	Melting, ~133 to 135 °C
	2, Isothermal, 135 °C for 1 h	-20.87	79.04	Weak
	3, Dynamic, 135 to 400 °C at 10 °C/min	-44.78 -29.92	34.26 4.34	Onset: 228.8 °C Onset: 336.1 °C
	4, Isothermal, 400 °C for 2 h	-0.63	3.71	Weak
Urea:Si (2:1 by mass)	1, Dynamic, 22 to 135 °C at 5 °C/min	-0.56	99.44	Melting ~133 to 135 °C
	2, Isothermal, 135 °C for 1 h	-33.77	65.67	Weak
	3, Dynamic, 135 to 400 °C at 10 °C/min	-18.38 -15.35	47.29 31.94	Onsets: 185.1 & 216.0 °C Onset: 299.4 °C
	4, Isothermal, 400 °C for 2 h	-0.41	31.53	Weak

PrSi remains essentially mass-stable throughout the full program, with no distinct DSC event (Figure 5a-c, Table I). This shows that PrSi undergoes no measurable mass loss or distinct thermal event under the applied conditions. Therefore, the mass-loss events observed for Urea:Si can be assigned primarily to urea-derived processes rather than degradation or volatilization of silicon.

Pure urea shows a multistep thermal response. During the initial heating to 135 °C, only negligible mass loss occurs, while the DSC trace displays the melting region near 133-135 °C (Figure 5b, Table I). During the subsequent 135 °C isothermal hold, however, urea loses ~20.9% of its initial mass. This shows that molten urea is not fully retained under the applied gas flow, even near its melting temperature. Such behavior is consistent with previous TG-MS studies

showing that below approximately 160 °C, urea decomposition is limited, but molten urea can evaporate slowly. At higher temperatures, urea decomposition becomes progressively more complex, involving NH_3, HNCO, biuret, cyanuric acid, and related condensed intermediates(Zhu et al., 2021).

The dynamic region in Figure 5c highlights the main difference between pure urea and the Urea:Si mixture. Pure urea undergoes two major mass-loss steps during heating from 135 to 400 °C. These are associated with DSC onsets at 228.8 °C and 336.1 °C and correspond to mass losses of ~44.8% and 29.9%, respectively (Table I). The first event is consistent with the main urea decomposition and volatilization stage, while the second is consistent with decomposition or removal of more stable condensed urea-derived residues. This assignment agrees with reported urea decomposition studies, where the first major mass-loss region occurs between roughly 140 and 250 °C, followed by further residue decomposition up to approximately 360-410 °C; cyanuric-acid-type species are especially relevant to the higher-temperature event, with rapid mass loss reported above approximately 330 °C (Tischer et al., 2019; Zhu et al., 2021).

In contrast, the Urea:Si mixture displays a shifted and redistributed thermal response. During the 135 °C isothermal stage, the mixture loses ~33.8% of its total mass, which corresponds to approximately half of the original urea fraction in the 2:1 Urea:Si mixture. This loss is substantially larger than for pure urea, indicating that the presence of silicon microparticles changes the physical state and retention of molten urea. A likely explanation is that molten urea spreads across the silicon particle surfaces and interparticle spaces, increasing its exposed area and accelerating evaporation or early transformation.

The DSC response in Figure 5c further supports this interpretation. Instead of the pure-urea onsets at 228.8 °C and 336.1 °C, the Urea:Si mixture shows features at 185.1 °C, 216.0 °C, and 299.4 °C. The corresponding TG losses during the dynamic ramp are ~18.4% and 15.4% (Table I). The lower-temperature events at 185.1 and 216.0 °C are consistent with decomposition or removal of remaining dispersed urea and early urea-derived intermediates. The later event at 299.4 °C is consistent with removal of more condensed urea-derived residues. Compared with pure urea, the shift to lower temperature indicates that these processes occur more readily when urea is distributed within the silicon powder bed. This may arise from thinner urea domains, greater gas exposure, stronger contact with silicon/native oxide surfaces, or reduced stability of condensed intermediates when formed in a dispersed state.

After the full program, the Urea:Si mixture retains ~31.5% of its initial mass, close to the theoretical silicon fraction of 33.3 wt% expected after complete removal of the urea-derived component from a 2:1 Urea:Si mixture. This agreement indicates that most of the urea-derived mass is removed by the end of the treatment, leaving silicon as the dominant solid residue. The small deviation from the theoretical value may reflect local mixture inhomogeneity, baseline correction, or minor physical loss during gas evolution.

Overall, the TG/DSC results show that urea-assisted porosification at 400 °C is not governed by a single decomposition event at the final temperature. Instead, the process begins during the 135 °C hold, where molten urea is partially lost or transformed, and continues through a shifted series of decomposition events between approximately 185 and 300 °C when urea is in contact with silicon. This observation also clarifies the role of the 400 °C condition identified in the previous temperature-screening study. That study compared atmospheric treatments at 220, 400, 600, and 800 °C and did not include an intermediate temperature between 300 and 400 °C. Thus, the present TG/DSC results do not imply that pore formation begins only at 400

°C; rather, they indicate that the principal urea-derived transformations occur during heating toward the final treatment temperature. The 400 °C condition should therefore be regarded as the previously identified processing endpoint at which the strongest atmospheric mesoporosity was obtained, while the active thermal sequence develops substantially below this temperature. This staged behavior is consistent with the strong influence of urea content on pore development, because the amount of urea controls not only the quantity of volatile species generated, but also the extent of molten-phase redistribution, intermediate formation, and removal within the silicon powder bed. Direct evolved-gas analysis, for example by TG-MS, gas-phase FTIR, or GC-MS, would be valuable in future work to verify the identities and temperature-dependent evolution of NH_3, HNCO, and other proposed urea-derived species.

3.5 Proposed mechanism of urea-assisted silicon porosification at 400 °C

The combined data suggest that porosification at 400 °C proceeds through a coupled thermal, chemical, and mechanical corrosion pathway. The process begins when molten urea redistributes through the Si powder bed during the 135 °C hold. In the Urea:Si mixture, this stage already removes a large fraction of the urea component, which is consistent with redistribution of the molten phase over Si surfaces and interparticle voids rather than its retention solely as a bulk urea pool. This redistribution is important because it may place urea-derived species directly at Si/SiO_x surfaces, grain boundaries, defects, and particle contacts, where pore formation is most likely to initiate.

Upon further heating, dispersed urea decomposes and produces NH_3 and HNCO, while secondary reactions generate biuret, cyanuric-acid-type species, and other condensed intermediates, as described by Reactions 1-5 in the Introduction.

These reactions are relevant because the intermediate region around 180-300 °C coincides with the temperature window where the Urea:Si mixture shows shifted DSC events and where the first major pore-opening processes are likely to occur. Previous studies of urea decomposition show that biuret, cyanuric acid, ammelide, and ammeline form through competing temperature-dependent pathways, and that biuret/urea-derived phases can pass through liquid, viscous, foam-like, or re-solidified states in the approximate 190-230 °C region (Schaber et al., 2004; Tischer et al., 2019; Zhu et al., 2021). In a powder bed, such transient phases can fill surface defects and interparticle constrictions, then expand, crystallize, decompose, or volatilize. This provides a plausible source of local stress, cracking, and cavity opening, consistent with the SEM and mercury intrusion observations.

The proposed chemical etching contribution may involve a local ammonia-water-oxygen-silicon oxide cycle. Although the present system is not an aqueous NH_4OH bath, it contains NH_3 from urea decomposition, oxygen from the air-containing atmosphere, and possible water from adsorbed moisture or urea-derived reactions. In such a microenvironment, NH_3 can act as a weak base:

$$NH_3 + H_2O \rightleftharpoons NH_4^+ + OH^- \quad (7)$$

The generated OH^- may then participate in alkaline attack of oxidized or hydroxylated silicon sites. A simplified alkaline silicon dissolution pathway can be written as:

$$Si + 2OH^- + 2H_2O \rightarrow Si(OH)_4 + 2e^- + H_2 \quad (8)$$

This type of reaction is consistent with ammonia-based silicon etching literature, where hydrogen evolution is used to quantify Si etch rates in NH_3 solutions and where dissolved oxygen strongly affects pit formation, surface roughness, and etching rate (Fukidome & Matsumura, 2000). Ammonia-peroxide cleaning studies also describe Si surface evolution as a competition between oxidation of Si and dissolution of the resulting oxide in alkaline media,

producing roughening when the formation and dissolution of hydrous silicon oxides are locally imbalanced (Knotter et al., 2000; Lee & Raghavan, 1999).

In the present process, we propose that O_2 does not simply passivate the surface. Instead, it may help generate oxidized or hydroxylated Si sites on freshly exposed surfaces, especially at defects, edges, cracks, and grain boundaries. These oxidized regions may then be destabilized or partially removed in the local NH_3/H_2O environment. Repetition of this oxidation-hydroxylation-dissolution cycle could preferentially attack high-energy regions rather than uniformly removing the whole particle. This is consistent with the EDS maps, where oxygen is enriched at edges and roughened regions, and with the progressive increase in O content as the urea loading increases. It may also help explain why pore formation is accompanied by oxygen incorporation rather than by clean removal of Si.

The role of the polycrystalline feedstock is also important. Polycrystalline Si contains grain boundaries, defects, and impurity-rich regions that are more chemically and mechanically vulnerable than ideal crystalline facets. Alkaline etching studies on polycrystalline Si have shown that grain boundaries and different crystal planes can etch preferentially, leading to interconnected porous structures (Yan et al., 2022). Therefore, in the Urea:Si system, urea-derived species likely exploit pre-existing heterogeneity in the metallurgical-grade Si. Initial cracking and oxide/hydroxide attack could expose fresh defect-rich surfaces, which may then undergo further localized modification. This could establish a reinforcing process in which cracking exposes new surface, newly exposed surface undergoes oxidation or hydroxylation, and chemically weakened regions become more susceptible to further opening.

Nitrogen incorporation may occur through surface reactions rather than bulk nitridation. NH_3 can interact with hydroxylated or oxidized Si surfaces through hydrogen bonding, acid-base interactions, or formation of aminosilicon/oxynitride-like surface motifs. Studies of SiO_2 and NH_3 show that NH_3 can form SiO_2–NH_3 complexes and $H_2NSiOOH$-type species, supporting the possibility of ammonia-derived modification of silica-like surface sites (Zhou & Chen, 2001). However, crystalline or stoichiometric Si_3N_4 formation generally requires much higher-temperature NH_3 treatments than used here; porous Si nitridation studies typically use NH_3 annealing above ~860 °C (Mei et al., 2022). Thus, the nitrogen-containing species reported previously for urea-treated Si are more plausibly assigned to surface-bound Si–N/Si–O–N-like environments, adsorbed or reacted urea fragments, NH_x-containing groups, or defect-associated nitrogen species rather than bulk silicon nitride formation.

The final pore architecture is therefore interpreted in terms of two cooperating contributions, consistent with our previous control experiments. The first contribution is chemical porosification, where $NH_3/H_2O/O_2$-derived local chemistry may modify, oxidize, hydroxylate, and partially dissolve vulnerable Si/SiO_x regions. This contribution is consistent with the BJH-resolved mesopore population near 4 nm and the oxygen-rich surfaces. The second contribution is mechanical pore opening, where gas evolution and transient urea-derived condensed phases may generate local pressure, swelling, cracking, and cavity formation. This contribution is consistent with the SEM-visible cracks and voids, the broader BJH feature in the ~80-100 nm range, and with the mercury-intrusion features in the 0.15 to 1 µm range. Together, these chemically and mechanically assisted processes provide a plausible explanation for the hierarchical structure observed in the present work, while the stronger experimental basis for separating these effects comes from the previous control study (Abo-Hamad et al., 2026).

This proposed mechanism is also consistent with the urea-loading dependence. At 0.5:1 and 1:1 Urea:Si, urea is sufficient to initiate surface roughening and mesopore formation, but the amount of molten phase and decomposition products is limited. At 2:1, urea appears sufficient to wet a large fraction of the powder bed and generate sustained local chemical and mechanical interactions, producing the large increase in BET surface area, pore volume, oxygen incorporation, and pore-network accessibility. Increasing the ratio to 4:1 gives only limited additional benefit, suggesting that the process becomes limited by Si surface accessibility, gas escape, intermediate removal, or local saturation of reactive sites rather than by urea availability alone. Excess urea may also decompose away from the Si surface or form transient condensed phases that do not contribute efficiently to pore generation.

Thus, the proposed 400 °C pathway is not simply a case of "urea decomposes and etches Si". A plausible interpretation is that molten urea first infiltrates and coats the Si powder bed; then NH_3/HNCO and condensed intermediates develop locally; oxygen and water may contribute to an oxide/hydroxide-mediated surface corrosion cycle; and simultaneous gas evolution plus intermediate expansion may assist the opening of cracks and cavities. The outcome is a porous, oxygen-enriched Si material in which mesopores and larger accessible pore/void features are consistent with contributions from the same coupled chemical-mechanical process.

From an implementation perspective, the use of commercially available Si powder, inexpensive urea, atmospheric-pressure processing, and a fluorine-free chemistry is favorable for future scale-up. The present process, however, remains a laboratory-scale batch treatment, and translation toward continuous processing would require further optimization of heat and mass transfer, gas handling, reagent utilization or recovery, and overall energy demand. Quantitative assessment of process economics and environmental impact will therefore be required before industrial deployment, and the present work should be regarded as an early-stage laboratory demonstration rather than an industrially validated process. The multiscale pore structure identified here may also be relevant to applications where accessible surface area, mass transport, and internal void space are important. In particular, these characteristics could be beneficial for Si-based battery electrodes and Si-carbon composites, as well as catalytic or other surface-driven applications. Application-specific performance, however, was not evaluated in the present study and requires dedicated investigation.

4. CONCLUSIONS

This study clarifies how urea content and staged thermal evolution govern fluorine-free porosification of polycrystalline Si microparticles at 400 °C. Increasing the Urea:Si ratio enhanced mesopore development up to 2:1, where the BET surface area reached 25.7 $m^2\ g^{-1}$ and the pore volume reached 0.039 $cm^3\ g^{-1}$. Further increasing the urea content to 4:1 gave only minor additional improvement, suggesting that pore formation may become limited by surface accessibility, gas transport, or intermediate removal rather than by urea availability alone.

The resulting porous Si is best described as a hierarchical, chemically modified structure rather than a simply etched powder. Nitrogen sorption revealed a dominant mesopore population near 4 nm together with a broader, less-defined contribution in the ~80-100 nm range, while mercury intrusion showed additional accessible pore/void features from approximately 0.15 µm to 1 µm. SEM and EDS further indicated that porosification is accompanied by surface roughening, cracking, cavity formation, and oxygen enrichment.

TG/DSC showed that the active transformation begins before the final 400 °C hold. In contact with Si, urea undergoes substantial loss during the 135 °C stage and displays decomposition

events shifted to lower temperatures than bulk urea. These findings are consistent with a proposed mechanism in which molten urea first redistributes through the powder bed, followed by localized generation of urea-derived species that may chemically modify Si/SiO_x surfaces while gas evolution and transient condensed phases may assist crack opening and pore formation.

Overall, the 400 °C route is not a single-temperature etching step, but a multistage porosification process controlled by the local contact between urea-derived phases and Si. The 2:1 Urea:Si condition provides a practical balance between reactivity and accessibility, providing a basis for further development toward scalable, fluorine-free production of porous silicon microparticles. Future work should focus on treatment-atmosphere optimization, particle-size and Si-purity effects, direct evolved-gas analysis, continuous processing and scale-up, and evaluation of electrochemical performance and long-term structural stability.

5. ACKNOWLEDGEMENTS

The authors gratefully acknowledge Vesta Si Sweden AB for providing the silicon microparticles and for access to facilities used for nitrogen sorption analysis. We also thank Pedro Berastegui at the Department of Chemistry, Ångström Laboratory, Uppsala University, for performing the TG/DSC measurements. Financial support from the Swedish Agency for Economic and Regional Growth and Region Västernorrland through the IMPHET project is gratefully acknowledged.

6. REFERENCES

Abo-Hamad, A., Phadatare, M., Brandell, D., Hahlin, M., & Örtegren, J. (2026). Porous Structuring of Si Microparticles for Li-Ion Battery Anodes by Urea-Assisted Etching. *ACS Omega*, *11*(8), 13902–13921. https://doi.org/10.1021/acsomega.5c12477

Abo-Hamad, A., Phadatare, M., Lindgren, F., Brandell, D., Hahlin, M., & Örtegren, J. (2025). Safe and cost-effective synthesis of porous silicon using Urea: Structural, morphological, and porosity analysis. *Microporous and Mesoporous Materials*, *397*, 113773. https://doi.org/10.1016/j.micromeso.2025.113773

Chen, L.-C., Chen, M., Tsaur, T.-H., Lien, C., & Wan, C.-C. (1995). Selective etching of silicon in aqueous ammonia solution. *Sensors and Actuators A: Physical*, *49*(1), 115–121. https://doi.org/10.1016/0924-4247(95)01007-N

Cheng, Z., Jiang, H., Zhang, X., Cheng, F., Wu, M., & Zhang, H. (2023). Fundamental Understanding and Facing Challenges in Structural Design of Porous Si-Based Anodes for Lithium-Ion Batteries. *Advanced Functional Materials*, *33*(26), 2301109. https://doi.org/10.1002/adfm.202301109

Fukidome, H., & Matsumura, M. (2000). Effect of dissolved oxygen on etching process of Si(111) in 2.5% NH3 solution. *Surface Science*, *463*(3), L649–L653. https://doi.org/10.1016/S0039-6028(00)00688-9

Kang, R. H., Baek, S. W., Oh, C.-K., Kim, Y. H., & Kim, D. (2025). Recent Advances of Macrostructural Porous Silicon for Biomedical Applications. *ACS Applied Materials & Interfaces*, *17*(4), 5609–5626. https://doi.org/10.1021/acsami.4c18296

Knotter, D. M., de Gendt, S., Mertens, P. W., & Heyns, M. M. (2000). Silicon Surface Roughening Mechanisms in Ammonia Hydrogen Peroxide Mixtures. *Journal of The Electrochemical Society*, *147*(2), 736. https://doi.org/10.1149/1.1393261

Lee, K. T., & Raghavan, S. (1999). Etch Rate of Silicon and Silicon Dioxide in Ammonia-Peroxide Solutions Measured by Quartz Xrystal Microbalance Technique. *Electrochemical and Solid-State Letters*, *2*(4), 172. https://doi.org/10.1149/1.1390773

Mei, S., Guo, S., Xiang, B., Deng, J., Fu, J., Zhang, X., Zheng, Y., Gao, B., Chu, P. K., & Huo, K. (2022). Enhanced ion conductivity and electrode–electrolyte interphase stability of porous Si anodes enabled by silicon nitride nanocoating for high-performance Li-ion batteries. *Journal of Energy Chemistry*, *69*, 616–625. https://doi.org/10.1016/j.jechem.2022.02.002

Moretta, R., De Stefano, L., Terracciano, M., & Rea, I. (2021). Porous Silicon Optical Devices: Recent Advances in Biosensing Applications. *Sensors*, *21*(4), 1336. https://doi.org/10.3390/s21041336

Nocerino, V., Rea, I., Siciliano, G., De Stefano, L., & Primiceri, E. (2024). Polymers modified porous silicon optical (bio)sensors. *TrAC Trends in Analytical Chemistry*, *177*, 117811. https://doi.org/10.1016/j.trac.2024.117811

Sánchez-Salcedo, R., Sharma, P., & Voelcker, N. H. (2025). Advancements in Porous Silicon Biosensors for Point of Care, Wearable, and Implantable Applications. *ACS Applied Materials & Interfaces*, *17*(2), 2814–2843. https://doi.org/10.1021/acsami.4c18273

Schaber, P. M., Colson, J., Higgins, S., Thielen, D., Anspach, B., & Brauer, J. (2004). Thermal decomposition (pyrolysis) of urea in an open reaction vessel. *Thermochimica Acta*, *424*(1), 131–142. https://doi.org/10.1016/j.tca.2004.05.018

Schnakenberg, U., Benecke, W., & Löchel, D. (1990). NH4OH-based etchants for silicon micromachining. *Proceedings of the 5th International Conference on Solid-State Sensors and Actuators and Eurosensors III*, *23*(1), 1031–1035. https://doi.org/10.1016/0924-4247(90)87084-V

Tischer, S., Börnhorst, M., Amsler, J., Schoch, G., & Deutschmann, O. (2019). Thermodynamics and reaction mechanism of urea decomposition. *Physical Chemistry Chemical Physics*, *21*(30), 16785–16797. https://doi.org/10.1039/C9CP01529A

Wang, M., Ou, W.-C., & Yu, Z.-T. (2025). Porous Silicon-Supported Catalytic Materials for Energy Conversion and Storage. *ChemSusChem*, *18*(3), e202401459. https://doi.org/10.1002/cssc.202401459

Wang, Y., & Wang, D. (2026). Advances in porous silicon materials for sensing, energy storage, and microelectronics. *Nanomaterials*, *16*(4), 257. https://doi.org/10.3390/nano16040257

Yan, Z., Jiang, J., Zhang, Y., Yang, D., & Du, N. (2022). Scalable and low-cost synthesis of porous silicon nanoparticles as high-performance lithium-ion battery anode. *Materials Today Nano*, *18*, 100175. https://doi.org/10.1016/j.mtnano.2022.100175

Zhou, M., & Chen, M. (2001). Reactions of silicon dioxide with ammonia molecules: Formation and characterization of the SiO2–NH3 complex and the H2NSiOOH molecule. *Chemical Physics Letters*, *349*(1), 64–70. https://doi.org/10.1016/S0009-2614(01)01192-7

Zhu, N., Qian, F., Xu, X., Wang, M., & Teng, Q. (2021). Thermogravimetric Experiment of Urea at Constant Temperatures. *Materials*, *14*(20). https://doi.org/10.3390/ma14206190

Ali Abo-Hamad
PhD Candidate, Engineering Physics, Mid Sweden University

Ali Abo-Hamad is a final-year PhD candidate in Engineering Physics at Mid Sweden University. He holds a Master of Engineering Science in Chemical Engineering and has previous industrial experience in the silicon sector. His research focuses on silicon-based materials, fluorine-free porous silicon synthesis, and surface/porosity engineering for functional applications. He has also worked on carbon nanomaterials, ionic liquids, deep eutectic solvents, and electrochemical sensor materials.
